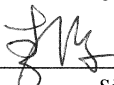**Kathryn I. Clark**

Quantification of CO$_2$ concentration in Apatite

submitted in partial fulfillment of the requirements for the degree of
Master of Science in Earth and Environmental Sciences
Department of Earth and Environmental Sciences
The University of Michigan

Accepted by:

_____   _____Youxue Zhang, Ph.D._____   Dec. 5, 2015
Signature   Name   Date

_____   _____Jie Li, Ph.D._____   Dec 04 2015
Signature   Name   Date

_____   Chris J. Poulsen   Dec 10 2015
Department Chair Signature   Name   Date

Earth and Environmental Sciences
MUNIVERSITY OF MICHIGAN

ABSTRACT

The infrared (IR) method for determining CO_2 concentrations in apatite was calibrated with absolute concentrations obtained through Nuclear Reaction Analysis (NRA). IR data were obtained on double-polished apatite samples of varying thickness using polarized transmission infrared spectroscopy. Due to the various sites and orientations of CO_3^{2-} in apatite, the IR spectra are complicated and do not have the same shape in different apatite samples. Hence, simple peak heights are not used to characterize CO_2 concentrations in apatite. The total absorbance (A_{total}) was derived using the integrated area under the curves in a given spectral region (for a given vibrational mode but typically include differently sited or oriented CO_3^{2-} subspecies). Then A_{total} is calculated as $A_{E//c}$ + $2A_{E\perp c}$ The calibration has been carried out for two wavenumber regions, one with high sensitivity and the other can be applied to apatite with high CO_2 concentrations. One calibration is for the fundamental asymmetric CO_3^{2-} stretching at wavenumbers of 1600-1300 cm^{-1}, and the CO_2 concentration in wt% can be obtained as $(7.56\pm0.36)\times10^{-6} A_{total}/d$ where d is sample thickness in cm. The fundamental stretching bands are strong and hence sensitive for measuring low CO_2 concentrations in apatite, down to ppm level. The second calibration is for the overtone CO_3^{2-} bands at wavenumbers of 2650-2350 cm^{-1}, and the CO_2 concentration in wt% is $(9.3\pm0.6)\times10^{-4} A_{total}/d$ where d is sample thickness in cm. The overtone bands are weak and hence are useful for measuring high CO_2 concentrations in apatite without preparation of super-thin wafers. The anisotropy is significant: difference between $A_{E//c}$ and $2A_{E\perp c}$ can reach a factor of 2.8. Hence, for high-accuracy, it is best to use polarized IR to determine CO_2 concentrations in apatite. For rough estimation, unpolarized IR spectra may be used by estimating $A_{total} = 3A_{unpol}$, where A_{unpol} is the average of integrated absorbance from unpolarized spectra.

Keywords: Carbonate in apatite, IR spectroscopy, nuclear reaction analysis, NRA

INTRODUCTION

The mineral apatite is a common accessory mineral found in terrestrial, martian and lunar rocks (e.g., McCubbin and Nekvasil 2008; Boyce et al. 2010; McCubbin et al. 2010a, 2010b, 2012) and is a common biomaterial. It has the ability to take numerous elements, including most volatile

2

elements, into its structure, depending on the composition of the surrounding milieu (Pan and Fleet 2002; Hughes and Rakovan 2015). The simplest formula of apatite is $Ca_5(PO_4)_3(OH)$, in which the Ca^{2+} site often contains Sr^{2+}, Ba^{2+}, Pb^{2+}, Na^+, and light rare earth elements, the P^{5+} site often contains As^{5+}, Si^{4+}, C^{4+}, and S^{6+}, and the OH^- site may be completely substituted by F^-, Cl^-, and/or CO_3^{2-}. Because of this, apatite serves as a good indicator of the conditions of the magmatic environment, especially volatile conditions, from which it forms. In particular, CO_2 concentration in apatite may be able to indicate CO_2 concentration or fugacity in terrestrial-lunar-martian magmas and metamorphic rocks. For this potential to be realized, it is essential to analyze CO_2 concentrations in small apatite crystals as well as zoning of CO_2 in apatite. The focus of this study is on the quantification of CO_2 concentrations in apatite by Fourier transform infrared spectroscopy (FTIR).

CO_2 enters apatite structure as carbonate ion CO_3^{2-} in a number of ways, resulting in complicated IR peaks originating from CO_3^{2-} in apatite (Tacker 2008). The CO_3^{2-} ion is a triangular plane ion, and may substitute into two different sites in apatite: the OH^- ion site and the PO_4^{3-} site. The former is referred to as the A site and the latter is referred to the B site for carbonate substitution (Fleet and Liu 2003; Fleet and Liu 2007; Fleet 2009). In the OH^- site, CO_3^{2-} may be oriented such that the bisector of the triangular CO_3^{2-} ion is parallel to **c**-axis of apatite (called type A1), or the bisector is perpendicular to the **c**-axis (called type A2) (Tacker 2008). Based on IR spectra, Tacker (2008) also identified two different sites of CO_3^{2-} ion in B site, and interpreted them to be due to alignment of the 3 oxygens of CO_3^{2-} onto oxygens of different triangular faces of the PO_4^{3-} tetrahedron (see also Ivanova et al. 2001). Each of these different substitutions results in slight changes in the apatite structure and lateral shifts in both the Raman and the IR bands. In addition, these substitutions are not mutually exclusive, and often occur in combination within the same crystal. This multitudinous substitution is most evident in the wavenumber region 1600-1300 cm^{-1}.

These substitutions are so complex that the IR signal from a single crystal can elicit as many as 7 peaks in this region (Tacker 2008).

There are a number of methods for assessing CO_2 concentrations in apatite (e.g., Gulbrandsen et al. 1966; Johnson and Maxwell 1981; Santos and Clayton 1995; Cassella et al. 2000; Marks et al. 2012; Grunenwald et al. 2014). Note that even though C in apatite is present as carbonate ion, here the concentration is referred to as CO_2 (wt% or ppm) that would be released if apatite were heated up to release all the volatiles, as is the convention. Previous methods are mostly bulk method, either by total carbon titration or total CO_2 release (Santos and Clayton 1995; Grunenwald et al. 2014), or KBr powder FTIR spectra (Santos and Clayton 1995; Marks et al. 2012; Grunenwald et al. 2014), or vapor phase FTIR spectra obtained by reacting 50 mg of apatite with HCl (Cassella et al. 2000). These methods typically require large samples, and even the most recent powder FTIR method by Grunenwald et al. (2014) still requires milligrams of apatite. Apatite crystal specimens are not always available in such large sizes. For example, in available samples from the Moon, apatite crystals are often in the range of tens of micrometers in size (Boyce et al. 2010; McCubbin et al. 2010). In addition, the powder or vapor FTIR methods (Santos and Clayton 1995; Cassella et al. 2000; Marks et al. 2012; Grunenwald et al. 2014) are destructive and not enough for the determination of heterogeneities at 100-µm scale. As demonstrated by Wang et al. (2011), IR signals of OH and carbonate of single apatite crystals are often very strong, and microbeam FTIR method on single apatite crystals has high sensitivity and precision in determining the OH and carbonate concentrations once calibrated. Wang et al. (2011) focused on polarized FTIR analyses of H_2O concentrations.

In this work, polarized micro-FTIR is used to quantify CO_2 concentrations in apatite. Although FTIR can be used to detect specific ion clusters (and in specific sites and orientations) in the crystal with high sensitivity and precision, to convert the resulting peak intensities to

4

concentrations an absolute concentration technique is needed for calibration. The creation of a calibration curve using large apatite crystals of varying concentrations would allow for future quantification of mineral content in smaller samples (Wang et al. 2011). Nuclear Reaction Analysis (NRA) is an effective way to determine the absolute concentrations of carbonate in large crystals (Mathez et al. 1987; Cherniak et al. 2010). The purpose of this project was to compare FTIR data with NRA quantification of carbonate in apatite from a variety of sources to build a calibration curve for the FTIR signatures in these crystals. However, one difficulty in using single crystal FTIR to quantify CO_2 concentrations in apatite is that the fundamental absorption bands are often too strong so that sometimes impractically too thin wafers must be prepared. To overcome the difficulty, appropriate combination bands that are orders of magnitude weaker can be used to determine CO_2 concentrations in apatite when the concentration is relatively high.

In addition to the high sensitivity and precision, another advantage of using polarized FTIR and assessing spectra when the **E**-vector is parallel or perpendicular to the **c**-axis of the crystal is improved accuracy in quantification of concentrations as well as revealing structural information (Libowitzky and Rossman 1996). It is interesting that with all the discussion of the importance of the alignment of CO_3 molecule with the **c**-axis of the apatite crystal (Fleet and Liu 2003; Fleet et al. 2004; Tacker 2008; Fleet 2009), the IR analysis of apatite parallel and perpendicular to the **c**-axis is quite rare (Suetsugu et al. 1998). Because of the different orientations of the carbonate, it is likely that the use of polarized FTIR will provide greater detail on the variety of substitutions, with some more prevalent when **E**//**c**, and others more prevalent when **E**⊥**c**, as well as more accurate quantification of CO_2 concentrations in apatite.

METHODS

Samples

Four apatite samples were obtained from various locations: Durango, Mexico (Cerro), High

Atlas Mountains, Morocco (HAM), Faraday Township, Ontario (Gulbrandsen et al. 1966) (ROM)

and one from an unknown location purchased from an online vendor (GEM). Two of these samples

(Cerro, HAM) have been used previously to calibrate the IR method to analyze H_2O concentrations

(Wang et al. 2011). All samples were mounted on glass slides with crystal bond and cut parallel to

the **c**-axis with a diamond wafering saw. Cerro and HAM are high-quality gem crystals with

excellent crystalline shape and are easy to cut into oriented wafers. ROM and GEM crystals are more

difficult to mount so as to be cut into oriented wafers because the original crystal surfaces are not

present. ROM was cut from a triangular prism crystal, resulting in a triangle face with dimensions of

6, 5.7, and 5.3mm on the three sides, respectively. GEM was originally nearly spherical so the

resulting face was an oval with a long diameter of 5.2 mm and a short diameter of 3.1 mm. These

samples were further cut into 2 pieces. One piece of each was used for NRA analysis and the other

was used for polarized micro-FTIR.

FTIR

For FTIR, samples were double polished at least three separate times to thicknesses ranging

from 1.4 mm to 20 μm. Sample thickness was determined using a Mitutoyo digital micrometer (with

a precision of ±1 μm and an accuracy of ±2 μm). For samples <100 μm, interference fringes in the

FTIR spectra were used to verify and determine thickness using the equation:

$$d = 1/(2n\Delta\omega), \tag{1}$$

6

where *d* is the thickness of the sample, *n* is the refractive index and $\Delta\omega$ is the period of the interference fringes in terms of wavenumbers. A refractive index of 1.65 was used.

Polarized spectra were obtained for both **E//c** and **E⊥c** on the single wafer cut parallel to the c-axis at the University of Michigan using a Perkin-Elmer Spectrum GX FTIR spectrometer with a microscope attachment, purged with N_2 gas. Spectra were acquired with a mid-infrared source, KBr beamsplitter, KRS-5 IR wire grid polarizer and a liquid nitrogen cooled MCT detector. An aperture of 50 μm by 50 μm was used. Data were recorded from 7800-700 cm^{-1}, with a resolution of 1 cm^{-1}.

The orientation to the **c**-axis was verified in each sample using the spectra near wavenumber 3540 (OH peak), which is zero when the **E⊥c** and maximal when **E//c** (Levitt and Condrate 1970; Wang et al. 2011). The peaks in apatite attributed to CO_3^{2-} were compared with polarized FTIR spectra of a double-polished crystal of calcite ($CaCO_3$).

Nuclear Reaction Analysis (NRA)

Nuclear Reaction Analysis (NRA) was used to determine absolute C concentrations in apatite (Mathez et al. 1987; Proust et al. 1994; Cherniak et al. 2010). The nuclear reaction is $^{12}C(d,p)^{13}C$ (i.e., $^{12}C + {}^{2}H \rightarrow {}^{13}C + {}^{1}H$) (Proust et al. 1994; Wang and Nastasi 2009; Csedreki et al. 2014). A high-energy beam of deuteron (^{2}H) particles bombards the target material (polished apatite crystal). As the particles go into the target, some ^{2}H particles react with the target nucleus (^{12}C), converting the target nucleus to a new nucleus (^{13}C) and releasing a reaction product (^{1}H) with a specific amount of energy. The released ^{1}H ion with different energy is detected in the NRA proton spectrum at different energy channels.

The samples prepared for NRA were polished with P-600 SiC sandpaper and 0.3 μm alumina powder on cloth. Samples were about 50 mm^2 in area and 1-3 mm thick. All NRA measurements

were carried out at the Michigan Ion Beam Laboratory (MIBL) at the University of Michigan with the 1.7 MV tandem accelerator. The deuteron beam energy was selected to be 1.31 MeV to maximize the $^{12}C(d,p)^{13}C$ nuclear reaction cross section (Wang and Nastasi 2009; Csedreki et al. 2014) and hence the signal in the spectrum to quantify the carbon concentration in the sample. An Si charged-particle detector with 15 keV energy resolution was used to acquire the spectrum. The detector was placed at a scattering angle of 135°. For the acquisition of the sample spectra a 17.7-μm thick Kapton ($H_{10}C_{22}N_2O_5$) foil was placed in front of the detector to filter out backscattered deuterons of low energy (< 1.1 MeV). This allowed for an increase in the deuteron current on the sample and decreased the acquisition times. The acquisition times were 500 seconds with deuteron current on the sample 130 nA. During the acquisition of the spectrum the direction of the deuteron beam is normal to the sample surface. The depth of the sample being probed was estimated using the SIMNRA software program (Mayer 1999). For the apatite samples, the depth was estimated to be ~6 μm.

Atomic carbon concentration was determined through NRA spectrum modeling also using the SIMNRA program (Mayer 1999). The NRA method is an absolute method and no independent calibration is necessary. Nonetheless, the procedure was verified by analyzing a calcite ($CaCO_3$), obtaining carbon concentration of 19.3±1.3 atomic%, in agreement with the stoichiometric concentration of carbon of 20 atomic%.

RESULTS

The NRA spectra and modeling curves are shown in Fig. 1. The peak at 2980 keV reflects surface carbon contamination and the data from 2600-2940 keV indicate carbon in the interior of the crystal. The detection limit of the NRA method is 0.113 wt% CO_2 and carbon concentration in some apatite is not high enough for NRA. For Cerro, the NRA signal is indistinguishable from the

background. Hence, For Cerro, the fitting quality is not high and the uncertainty in modeling the carbon concentration is large. In order to determine concentrations better, constraints from FTIR spectra are used to estimate the background in NRA and subtract the same background counts from the NRA signals of all samples. Based on IR spectra in the v3 region (see later sections), the integrated absorbace A_{total} (see eq. (2)) for Cerro is ~1/5 of that for HAM. Because A_{total} is proportional to carbon concentration, a background to the NRA spectra is assigned so that carbon concentration in Cerro is ~1/5 of that for HAM. The resulting carbon concentration in ROM, GEM, HAM and Cerro are listed in Table 1. The CO_2 concentration in the ROM apatite grain that was analyzed by NRA is 0.66±0.06 wt% (1σ error) based on NRA analysis, not too different from 0.57 wt% obtained by Gulbrandsen et al. (1966) who analyzed bulk apatite crystals from the same location.

Typical IR spectra with the **E** vector parallel and perpendicular to the **c**-axis are shown in Fig. 2. Band identifications were taken from Regnier et al. (1994) and Koleva and Petkova (2012). The bands due to PO_4 at ~1000 cm^{-1} are typically oversaturated. Oversaturation is indicated when the peak is at high absorbance values and when the peak region is not smooth, but shows a lot of "noise". These data are not useable for any kind of quantification. The bands at ~2000 cm^{-1} are due to overtones of PO_4. The OH band at 3540 cm^{-1} is highly anisotropic, with zero intensity when **E**//**c**, and is used to verify the orientation of the samples. Among the fundamental carbonate vibrational modes, v3 (double-degenerate antisymmetric stretch in the region of 1600-1300 cm^{-1}) is well separated from other bands and suited for the quantification of CO_2 concentration. The v2 mode (out-of-plane bend in the region of 850-900 cm^{-1}) is close to the main PO_4 bands, and oversaturated, making it difficult to use. There are numerous carbonate v3 and v2 bands in apatite due to different carbonate substitution (A1, A2, B1 and B2, Tacker 2008). The v1 mode is IR-inactive and v4 (at

9

~720 cm^{-1}) is not always present. Hence, among the fundamental vibration modes, the v3 bands are calibrated in this study.

The v3 infrared bands are strong and easily oversaturated. In the current study, some apatite with high CO_2 concentration was specifically chosen because NRA requires high concentrations. Hence, to avoid supersaturation of the IR bands, the samples must be very thin, and the thinnest sample is only 20 μm thick for ROM which has the highest CO_2 concentration. That is, these IR bands have high sensitivity and are good for obtaining low CO_2 concentrations in apatite once calibrated but are not convenient for quantifying high CO_2 concentrations (e.g., ≥ 1000 ppm). To overcome this difficulty, the bands for carbonate are also calibrated in apatite in the region of 2650-2350 cm^{-1} (tentatively assigned as the first overtone of v3). The bands in this region are about two orders of magnitude weaker than these in 1600-1300 cm^{-1}, can only be clearly resolved when the samples are greater than 0.5 mm thick (Fig. 3), and are hence well suited when CO_2 concentration is high in apatite.

To view the IR bands more clearly, the left 3 panels of Figure 3 illustrate the spectra in the region of 1600-1300 cm^{-1} for **E** vector parallel or perpendicular to the **c**-axis of the apatite crystal. The shapes of the peaks are variable from one apatite crystal to another, with major and minor peaks. For ROM and GEM apatite crystals, there are major double peaks at 1455 and 1428 cm^{-1}. When **E**⊥**c**, the two peaks are nearly identical, and when **E**//**c**, these peaks become uneven in height. The right 3 panels of Figure 3 show the same information in the region of 2650-2350 cm^{-1}. Often the absorbance for **E**⊥**c** is larger than that for **E**//**c**, but for Cerro, the opposite is true. It can be seen that the spectra shape in the region of 2650-2350 cm^{-1} is similar to that in the region of 1600-1300, and these peaks are tentatively assigned to be the first overtone of the various v3 peaks in the region of 1600-1300 cm^{-1}.

The carbonate peaks in the 1600-1300 cm^{-1} range and the 2650-2350 cm^{-1} range are consistent with peaks observed in the calcite samples herein as well as with those observed by others (Adler and Kerr 1962; Gunasekaran et al. 2006) but the spectra of carbonate in apatite are more complicated due to the lifting of the double degeneracy and the multiple sites and orientations for the substitution of CO_3 group into the apatite structure. Specifically, the shape of the spectra is related to the relative abundances of CO_3 groups in different sites and orientations, and is variable (e.g., comparing ROM with HAM). Therefore, the simple approach of using linear absorbance of main peaks (e.g., Wang et al. 2011) does not work well, so the integrated absorbance over each region is used to quantify the CO_2 concentration in apatite.

Calibration

The data in Table 1 are used to calibrate the FTIR technique for the analysis of CO_2 concentration in apatite. The calibration is based on Beer's law describing the relationship between CO_2 concentration and FTIR absorbance as:

$$C = \alpha A_{total}/d, \qquad\qquad (2)$$

where C is CO_2 concentration, A_{total} ($= A_{E//c} + 2A_{E\perp c}$ because there are two principal axes that are perpendicular to the **c**-axis and one that is parallel to the **c**-axis) is the total integrated absorbance of the IR band in the wavenumber region of either 1600-1300 cm^{-1} or 2650-2350 cm^{-1}, with total meaning summation over three crystallographic directions, d is the sample thickness, and α is a constant that contains the molar mass of CO_2, the density of apatite and the integrated molar absorptivity in a specific spectrum region. For the units, the unit of A_{total} is the same as that of the

wavenumber (cm^{-1}), and the unit of d is chosen to be cm, and the unit of C is chosen to be wt% CO_2

(C =1 means 1 wt% of CO_2). Hence, the unit of α is wt%·cm^2.

Because of the multiple possible peaks due to variations in the substitution of the CO_3^{2-} ion

(Regnier et al. 1994; Fleet and Liu 2004; Fleet et al. 2004), the integrated area between the curve and

the baseline was used as the characteristic to represent CO_2 concentration in apatite. To obtain the

baseline, a regression line was created that formed a tangent across the lowest point on either side of

the bands defining the peaks in the wavenumber range (1600-1300 or 2650-2350 cm^{-1}) (Figure 4).

For the 1600-1300 cm^{-1} region, the lowest points are near 1580 cm^{-1} and 1360 cm^{-1} (with some

variability), respectively. For the 2650-2350 cm^{-1} region, the lowest points are near 2580 cm^{-1} and

2405 m^{-1}. Then the baseline is subtracted from the spectrum. The total area of all the bands in a

region between the two tangential points is obtained by numerical integration $\int A d\omega$ from one

tangential point to the other. This is done for both the $\mathbf{E} \perp \mathbf{c}$ spectrum to obtain $A_{\mathbf{E} \perp \mathbf{c}}$ (the integrated

absorbance for $\mathbf{E} \perp \mathbf{c}$) and for the $\mathbf{E} // \mathbf{c}$ spectrum to obtain $A_{\mathbf{E} // \mathbf{c}}$ (the integrated absorbance for $\mathbf{E} // \mathbf{c}$).

Then A_{total} is calculated as $A_{\mathbf{E} // \mathbf{c}} + 2 A_{\mathbf{E} \perp \mathbf{c}}$. The $A_{\mathbf{E} \perp \mathbf{c}}$, $A_{\mathbf{E} // \mathbf{c}}$, and A_{total} of all samples are listed in Table 1.

For convenience, the integrated absorbance in the 1600-1300 cm^{-1} region is referred to as A_{1440}, and

that in the 2650-2350 cm^{-1} region is referred to as A_{2500}. It can be seen that per sample thickness,

A_{total} in the 2650-2350 cm^{-1} region is about 0.8% of that in the 1300-1600 cm^{-1} region.

Figure 5 illustrates the calibration curve for NRA (wt%) vs integrated area of the FTIR signal

at wavenumbers 1600-1300 cm^{-1} (a) and wavenumbers 2650-2350 cm^{-1} (b). The data are fit by

equation (2) (i.e., the intercept is forced to be zero) to obtain α using the York algorithm (York 1969)

but forcing the intercept to be zero. The Cerro sample is plotted but not used in the fitting because it

has already been used in estimating the background for NRA. For the 1600-1300 cm^{-1} region (v3

bands), the fit value and 1σ error for the slope α (Fig. 5a) is:

$$\alpha_{1600-1300} = (7.56 \pm 0.36) \times 10^{-6} \text{ wt\% \cdot cm}^2, \quad \text{MSWD} = 0.88. \quad\quad (2a)$$

For the 2650-2350 cm^{-1} region, the fit (Fig. 5b) gives:

$$\alpha_{2650-2350} = (9.3 \pm 0.6) \times 10^{-4} \text{ wt\% \cdot cm}^2, \quad \text{MSWD} = 2.64. \quad\quad (2b)$$

The mean square weighted deviation (MSWD) is larger than 1, probably reflecting the difficulty of integrating the smaller peaks over a wide range of wavenumbers.

On the basis of 2σ reproducibility of IR spectra, the detection limit of the integrated absorbance is of the order 1 cm^{-1}. Therefore, the detection limit for infrared measurement of CO_2 in apatite using the v3 bands can be sub-ppm for 1-mm thick apatite samples. For 0.1-mm thick apatite crystals, the detection limit is about 8 ppm. That is, the v3 bands are very sensitive for quantitative measurements of CO_2 in apatite using polarized IR on oriented crystals, but very thin wafers must be prepared when the CO_2 concentration is > 0.1 wt%. On the other hand, for a 1-mm thick apatite crystal, the detection limit using the bands in the 2650-2350 cm^{-1} region is about 100 ppm, and wt% level CO_2 concentrations can be measured using these bands.

H_2O concentration in the apatite samples

The IR data also provide information on H_2O concentration using the calibration of Wang et al. (2011). All the spectra show a dominant peak at 3540 cm^{-1} for OH in apatite, and hence simple linear absorbance can be used to obtain H_2O concentration. For HAM and Cerro, the peak at 3540 cm^{-1} was oversaturated (the samples were not thin enough for the OH peak because no special effort was made to obtain OH concentrations). Wang et al. (2011) reported H_2O concentrations of 0.44 and 0.085 wt% for HAM and Cerro, respectively. For ROM and GEM, the H_2O concentrations so

obtained are shown in Table 1. It can be seen that ROM has the lowest H_2O but the highest CO_2 concentration among the samples. The GEM crystal for this study has lower H_2O concentration compared to Gem3 and Gem4 used in Wang et al. (2011).

DISCUSSION

The various peaks in the v3 region

The substitution of CO_3^{2-} into the apatite crystal is complex (El Feki et al. 1999; Comodi and Liu 2000; Ivanova et al. 2001; Leventouri et al. 2001; Fleet and Liu 2003, 2004, 2005; Fleet et al. 2004; Antonakos et al. 2007; Koleva and Petkova 2012). As summarized by Tacker (2008), CO_3^{2-} can substitute on the OH (or Cl or F) site (Type A) as well as on a PO_4^{3-} site (Type B). Type A substitutions occur in two different forms (Fleet et al. 2004). Using X-ray structural analysis, Fleet and Liu (2003) and Fleet et al. (2004) discovered an A-type substitution ordered along the apatite channel, which they labeled A1 because they also identified a second Type A substitution in a "stuffed" position which apparently acts as a charge balance for a B-type substitution (A2). The different Type A substitutions are reflected by different bands in the IR spectrum, with A1 bands at 1541 and 1449 cm^{-1} and A2 bands at 1563 and 1506 cm^{-1} (Fleet et al. 2004). The Type B substitutions also occur in two different forms. According to Tacker (2008), the B1 substitution is on one face of the PO_4 molecule, while the B2 substitution is on a different face with resulting IR spectral bands at 1450 and 1409 cm^{-1} (B1) and 1460 and 1427 cm^{-1} (B2).

14

The complication of identification is evident in the overlapping of these bands in the IR spectra between 1460 and 1445 cm^{-1}. One benefit of using polished single crystals and polarized spectra is the ability to pull out details of these differing substitutions.

The utility of using polarized vectors parallel and perpendicular to the c-axis of the crystal is evident in Figure 6. When $\mathbf{E} \perp \mathbf{c}$, the two major peaks are similar in height. When $\mathbf{E}//\mathbf{c}$, the band at 1428 cm^{-1} is smaller in height relative to the band at 1455 cm^{-1}. This would imply that the band at 1428 cm^{-1} is reflecting the activity of a substitution that is at a high angle to the **c**-axis and thus decreases when the energy is parallel to **c** (B2). The band at ~1406 cm^{-1} has been identified as a B1 signal, which corresponds to v3a in Fleet et al. (2004), parallel to the **c**-axis. There are other subtle differences between perpendicular and parallel spectra, with small shoulders appearing at the wavenumbers identified by Tacker (2008) as the four substitution sites. For example, the A1 substitution is stronger at 1455 cm^{-1} (combined with the B2 substitution) and disappears at higher wavenumbers. The A1 substitution at these higher wavenumbers is evident only when $\mathbf{E}//\mathbf{c}$. The A2 substitution is visible only when $\mathbf{E} \perp \mathbf{c}$, which is consistent with integration in the columnar anion (F$^-$, Cl$^-$, OH$^-$) perpendicular to the c-axis (Fleet et al. 2004; Tacker 2008). The IR bands for B1 and B2 substitutions are at lower wavenumbers than those for the A1 and A2 substitutions.

In addition to being able to identify the multiple substitutions that are made by CO_3^{2-} into apatite, which is aided by the use of spectra from both parallel and perpendicular energy, the integrated area of the entirety from these wavenumbers can be used to quantify the amount of CO_3^{2-} in the crystal using a calibration curve. An implicit assumption is that all the subspecies have the same integrated molar absorptivity. Note these are all subspecies of CO_3^{2-}, not the chemically different species such as CO_3^{2-} and CO_2, or OH and H_2O. Even for major species of the same element, the molar absorptivities are not very different. For example, Newman et al. (1986) estimated that for two major species of H (hydroxyl group OH$^-$ and neutral molecule of H_2O) in

rhyolitic glasses, the integrated molar absorptivity for OH is 1.67 times that for H_2O at the 3550 cm^{-1} band, and 0.83 times that for H_2O at the 4000 cm^{-1} band, and 1.16 times that for H_2O at the 7100 cm^{-1} band. On the other hand, Leschik et al. (2004) cautioned that it is difficult to verify whether the results in Newman et al. (1986) are due to difference in the molar absorptivities or due to structural variations, meaning that molar absorptivities of different H species may be roughly identical. Furthermore, it is expected that the integrated molar absorptivities of differently positioned or oriented CO_3^{2-} are more similar than the different chemical species of OH^- and H_2O. Hence, the assumption that the differently sited or oriented CO_3^{2-} subspecies have the same integrated molar absorptivity is reasonable although future high-precision work is needed to distinguish small differences in integrated molar absorptivities for different CO_3^{2-} subspecies.

Once the various substitutions of CO_3^{2-} into apatite are understood and the peak positions well quantified, it may be possible to deconvolute the various peaks in Figure 6 and use them to quantify the concentrations of each type and subtype of CO_3^{2-} substitution in apatite (Comodi and Liu 2000). The relative concentrations of the various subspecies may depend on temperature, pressure, melt composition such as the availability of P and F-OH-Cl, and other ambient conditions. If the controlling factors for the different substitutions are understood, the deconvoluted concentrations of the CO_3^{2-} subspecies might be able to provide rich information on apatite formation conditions.

Using unpolarized spectra to roughly estimate CO_2 concentrations in apatite

Because apatite is ubiquitous in both geological (Harlov 2015; Hughes and Rakovan 2015) and biological systems (Grunenwald et al. 2014), the use of these calibrations may be widespread. One advantage of calibrating for both lower (1600-1300 cm^{-1}) and higher (2650-2450 cm^{-1}) wavenumbers is that samples with higher carbonate content (as in biological samples) do not have to be thinned to <100 μm in order to quantify the carbonate concentration.

Often apatite crystals are small or otherwise difficult to orient. For CO_3^{2-} in apatite, at least

for the four samples studied in this work, the degree of anisotropy is not very large, with the ratio of

$A_{//c}/A_{\perp c}$ ranging from 0.47 to 2.73 for the 1600-1300 cm^{-1} bands, not too different from 1. This is in

contrast to the OH band at 3540 cm^{-1} in apatite, which is completely anisotropic, with the ratio of

$A_{//c}/A_{\perp c}$ being infinity. The smaller degree of anisotropy means that CO_2 concentration in apatite may

be roughly estimated using unpolarized spectra on unoriented apatite crystals. Such rough estimation

can be achieved by measuring a couple of unpolarized spectra on unoriented apatite sections, finding

the average integrated absorbance, multiplying it by 3 to estimate the total integrated absorbance

(A_{total}), and then using eq. (2) and the appropriate value of α to estimate the CO_2 concentration.

Consider the range of $A_{//c}/A_{\perp c}$ ratios from 0.47 to 2.73 as observed in this study for the 1600-1300 cm^{-1}

bands. If the ratio of $A_{//c}/A_{\perp c} = 0.47$, then using a single unpolarized spectrum of a random section

would lead to an estimated A_{total} to be 0.57 to 1.21 times the true A_{total}. If the ratio of $A_{//c}/A_{\perp c} = 2.73$,

then using a single unpolarized spectrum of a random section would lead to an estimated A_{total} to be

0.63 to 1.73 times the true A_{total}. Combining these results, the estimated A_{total} and CO_2 content would

be 0.57 to 1.72 times the true values using one unpolarized IR spectrum on a random section.

Measuring and averaging two or more randomly oriented sections would reduce the uncertainty

significantly.

The detail of the data is evident in these natural samples that are double polished and analyzed

using polarized FTIR. In addition to being able to identify the multiple substitutions that are made by

CO_3^{2-} into apatite, which is aided by the use of spectra from both parallel and perpendicular energy,

the integrated area of the entirety from these wavenumbers can be used to quantify the amount of

CO_3^{2-} in the crystal using a calibration curve. While this calibration curve can be roughly used with

unoriented samples, more work is necessary to verify the utility of such a curve on samples that are

prepared as KBr pellets.

ACKNOWLEDGMENTS

REFERENCES CITED

Adler, H. and Kerr, P. (1962) Infrared study of Aragonite and Calcite. American Mineralogist, 5-6

Antonakos, A., Liarokapis, E. and Leventouri, T. (2007) Micro-Raman and FTIR studies of synthetic and natural apatites. Biomaterials, 28, 3043-3054

Boyce, J.W., Liu, Y., Rossman, G.R., Guan, Y., Eiler, J.M., Stolper, E.M. and Taylor, L.A. (2010) Lunar apatite with terrestrial volatile abundances. Nature, 7305, 466-U2

Cassella, A., de Campos, R., Garrigues, S., de la Guardia, M. and Rossi, A. (2000) Fourier transform infrared determination of CO_2 evolved from carbonate in carbonated apatites. Fresenius Journal of Analytical Chemistry, 367, 556-561

Cherniak, D.J., Hervig, R.L., Koepke, J., Zhang, Y., and Zhao, D. (2010) Analytical methods in diffusion studies. Rev. Mineral. Geochem., 72, 107-170

Comodi, P. and Liu, Y. (2000) CO_3 substitution in apatite: further insight from new crystal-chemical data of Kasekere (Uganda) apatite. European Journal of Mineralogy, 5, 965-974

Csedreki, L., Uzonyi, I., Sziki, G.A., Szikszai, Z., Gyurky, G., and Kiss, A.Z. (2014) Measurements and assessment of $^{12}C(d,p\gamma)^{13}C$ reaction cross sections in the deuteron energy range 740-2000 keV for analytical applications. Nuclear Instruments and Methods in Physics Research Section B: Beam Interactions with Materials and Atoms, 328, 59-64

El Feki, H., Savariault, J.M. and Ben Salah, A. (1999) Structure refinements by the Rietveld method of partially substituted hydroxyapatite: Ca9Na0.5(PO4)(4.5)(CO3)(1.5)(OH)(2). Journal of Alloys and Compounds, 1-2, 114-120

Fleet, M.E., and Liu, X.Y. (2003) Carbonate apatite type A synthesized at high pressure: new space group (P-3) and orientation of channel carbonate ion. Journal of Solid State Chemistry, 174, 412-417

Fleet, M.E., and Liu, X.Y. (2004) Location of type B carbonate ion in type A-B carbonate apatite synthesized at high pressure. Journal of Solid State Chemistry, 177, 3174-3182

Fleet, M.E. and Liu, X.Y. (2005) Local structure of channel ions in carbonate apatite. Biomaterials, 36, 7548-7554

Fleet, M., Liu, X. and King, P. (2004) Accommodation of the carbonate ion in apatite: An FTIR and X-ray structure study of crystals synthesized at 2-4 GPa. American Mineralogist, 89, 1422-1432

Fleet, M.E., and Liu, X. (2007) Coupled substitution of type A and B carbonate in sodium-bearing apatite. Biomaterials, 28, 916-926.

Fleet, M.E. (2009) Infrared spectra of carbonate apatites: v(2)-Region bands. Biomaterials, 8, 1473-1481

Grunenwald, A., Keyser, C., Sautereau, A.M., Crubezy, E., Ludes, B. and Drouet, C. (2014) Revisiting carbonate quantification in apatite (bio)minerals: a validated FTIR methodology. Journal of Archaeological Science, 49, 134-141

Gulbrandsen, R.A., Kramer, J.R., Beatty, L.B., and Mays, R.E. (1966) Carbonate-bearing apatite from Faraday Township, Ontario, Canada. Am. Mineral., 51, 819-824.

Gunasekaran, S., Anbalagan, G. and Pandi, S. (2006) Raman and infrares spectra of carbonates of calcite structure. Journal of Raman Spectroscopy, 9, 892-899

Harlov, D.E. (2015) Apatite: a fingerprint for metasomatic processes. Elements, 3, 171-176.

Hughes, J.M. and Rakovan, J.F. (2015) Structurally robust, chemically diverse: Apatite and apatite supergroup minerals. Elements, 3, 165-170

Ivanova, T., Frank-Kamenetskaya, O., Kol'tsov, A. and Ugolkov, V. (2001) Crystal structure of calcium-deficient carbonated hydroxyapatite. Thermal decomposition. Journal of Solid State Chemistry, 2, 340-349

Johnson, W.M., and Maxwell, J.A. (1981) Rock and Mineral Analysis. 506 p. Wiley & Sons, New York.

Koleva, V. and Petkova, V. (2012) IR spectroscopic study of high energy activated Tunisian phosphorite. Vibrational Spectroscopy, 58, 125-132

Leschik, M., Heide, G., Frischat, G.H., Behrens, H., Wiedenbeck, M., Wagner, N., Heide, K., Geissler, H., and Reinholz, U. (2004) Determination of H_2O and D_2O contents in rhyolitic glasses using KFT, NRA, EGA, IR spectroscopy, and SIMS. Phys. Chem. Glasses, 45, 238-251.

Leventouri, T., Chakoumakos, B.C., Papanearchou, N. and Perdikatsis, V. (2001) Comparison of crystal structure parameters of natural and synthetic apatites from neutron powder diffraction. Journal of Materials Research, 9, 2600-2606

Levitt, S.R., and Condrate Sr., R.A. (1970) The polarized infrared spectra of hydroxyl ion in fluorapatite. Appl. Spectroscopy, 24, 288-289.

Libowitzky, E. and Rossman, G. (1996) Principles of quantitative absorbance measurements in anisotropic crystals. Physics and Chemistry of Minerals, 6, 319-327

Marks, M.A.W., Wenzel, T., Whitehouse, M.J., Loose, M., Zack, T., Barth, M., Worgard, L., Krasz, V., Eby, G.N., Stosnach, H. and Markl, G. (2012) The volatile inventory (F, Cl, Br, S, C) of magmatic apatite: An integrated analytical approach. Chemical Geology, 241-255

Mathez, E., Blacic, J., Beery, J., Hollander, M. and Maggieore, C. (1987) Carbon in olivine - results from Nuclear-Reaction Analysis. Journal of Geophysical Research-Solid Earth and Planets, B5, 3500-3506

Mayer, M. (1999) SIMNRA, a simulation program for the analysis of NRA, RBS and ERDA. In Application of Accelerators in Research and Industry, Pts 1 and 2, vol. 475, p. 541-544. AIP Conference Proceedings, American Institute of Physics, Melville, New York.

McCubbin, F.M. and Nekvasil, H. (2008) Maskelynite-hosted apatite in the Chassigny meteorite: Insights into late-stage magmatic volatile evolution in martian magmas. American Mineralogist, 4, 676-684

McCubbin, F.M., Hauri, E.H., Elardo, S.M., Vander Kaaden, K.E., Wang, J. and Shearer, C.K.,Jr. (2012) Hydrous melting of the martian mantle produced both depleted and enriched shergottites. Geology, 8, 683-686

McCubbin, F.M., Steele, A., Hauri, E.H., Nekvasil, H., Yamashita, S. and Hemley, R.J. (2010a) Nominally hydrous magmatism on the Moon. Proceedings of the National Academy of Sciences of the United States of America, 25, 11223-11228

McCubbin, F.M., Steele, A., Nekvasil, H., Schnieders, A., Rose, T., Fries, M., Carpenter, P.K. and Jolliff, B.L. (2010b) Detection of structurally bound hydroxyl in fluorapatite from Apollo Mare basalt 15058,128 using TOF-SIMS. American Mineralogist, 8-9, 1141-1150

Newman, S., Stolper, E.M., and Epstein, S. (1986) Measurement of water in rhyolitic glasses: calibration of an infrared spectroscopic technique. Am. Mineral., 71, 1527-1541.

Pan, Y. and Fleet, M. (2002) Compositions of the apatite-group minerals: Substitution mechanisms and controlling factors. Phosphates: Geochemical, Geobiological, and Materials Importance, 13-49

Proust, C., Husson, E., Blondiaux, G. and Coutures, J.P. (1994) Residual Carbon Detection in Barium-Titanate Ceramics by Nuclear-Reaction Technique. Journal of the European Ceramic Society, 3, 215-219

Regnier, P., Lasaga, A., Berner, R., Han, O. and Zilm, K. (1994) Mechanism of (CO_3)-O-2-substitution in Carbonate-Fluorapatite - Evidence from FTIR spectroscopy, C-13 Nmr, and quantum-mechanical calculations. American Mineralogist, 9-10, 809-818 ER

Santos, R.V. and Clayton, R.N. (1995) The carbonate content in high-temperature apatite - an analytical method applied to apatite from the Jacupiranga Alkaline Complex. American Mineralogist, 3-4, 336-344

Suetsugu, Y., Shimoya, I. and Tanaka, J. (1998) Configuration of carbonate ions in apatite structure determined by polarized infrared spectroscopy. Journal of the American Ceramic Society, 3, 746-748 ER

Tacker, R.C. (2008) Carbonate in igneous and metamorphic fluorapatite: Two type A and two type B substitutions. American Mineralogist, 1, 168-176

Wang, K.L., Zhang, Y. and Naab, F.U. (2011) Calibration for IR measurements of OH in apatite. American Mineralogist, 8-9, 1392-1397

Wang, Y. and Nastasi, M. (editors) (2009) Handbook of Modern Ion Beam Materials Analysis, 2nd Edition, Published by Material Research Society

York, D. (1969) Least-squares fitting of a straight line with correlated errors. Earth and Planetary Science Letters, 5, 320-324

Table 1. NRA and FTIR data on apatite

Apatite	H_2O wt%	CO_2 wt%	A_{1440} E⊥c	A_{1440} E//c	A_{1440} total	A_{2500} E⊥c	A_{2500} E//c	A_{2500} total
ROM	0.043±0.008	0.664±0.055	37250	17380	91870	323±17	125±3	772±34
GEM	0.24±0.01	0.181±0.040	8890±52	6590±263	24380±159	64.5±1.3	27.5±0.7	157±3
HAM	--	0.142±0.034	5018±270	5438±134	15474±674	43.7±1.3	31.6±1.3	119.1±1.2
Cerro	--	0.028±0.012	683	1868	3234	--	--	--

Note: H_2O concentration is based on IR measurement in this study using the calibration of Wang et al. (2011). CO_2 concentration is based on NRA analyses in this study, except for Cerro, for which the CO_2 concentration was estimated using the relationship between total absorbance of Cerro and the total absorbance of HAM (see text). Because of this, the CO_2 values of Cerro are not used in the calibration. The absorbances are integrated absorbances per cm thickness. For Cerro, the CO_2 concentration is low and hence A_{2500} cannot be determined well.
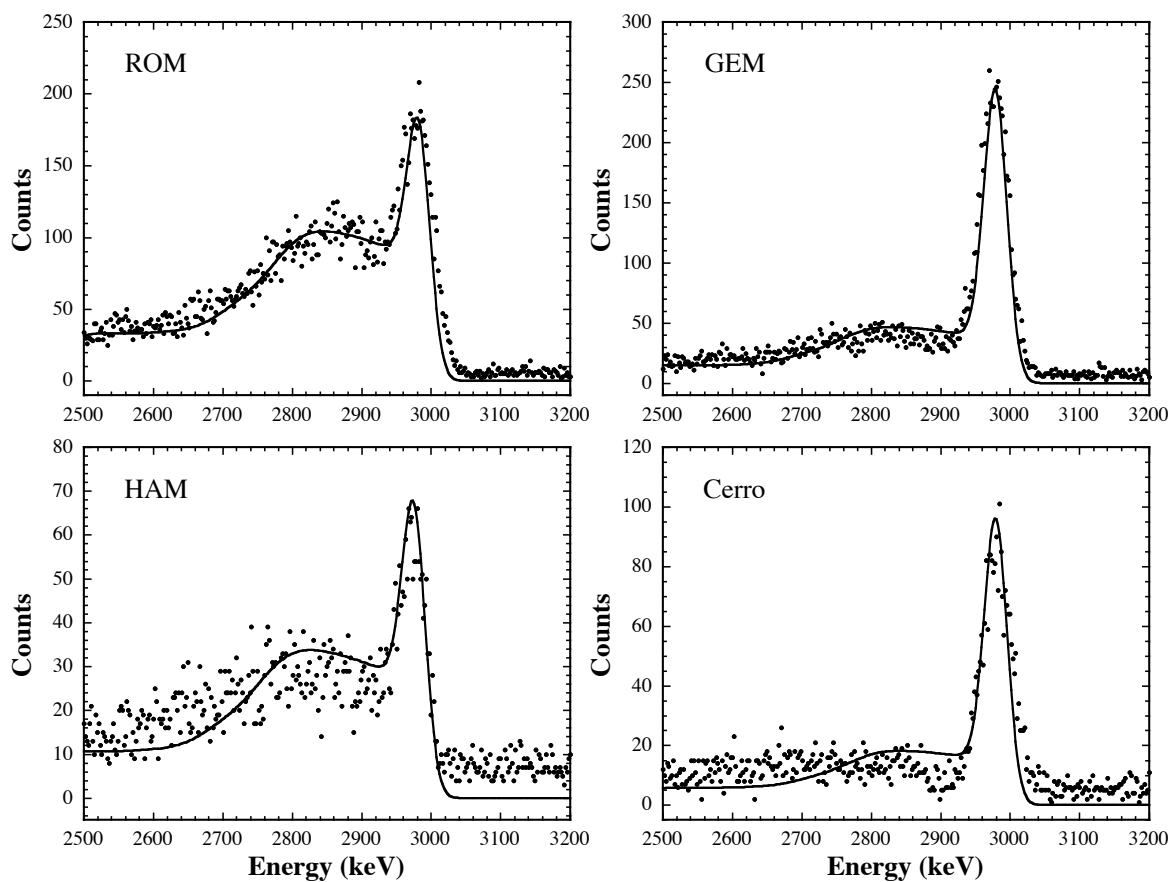
Fig. 1. NRA spectra of four samples. The points are data and the curves are modeling of the data using the SIMNRA software (Mayer, 1999).
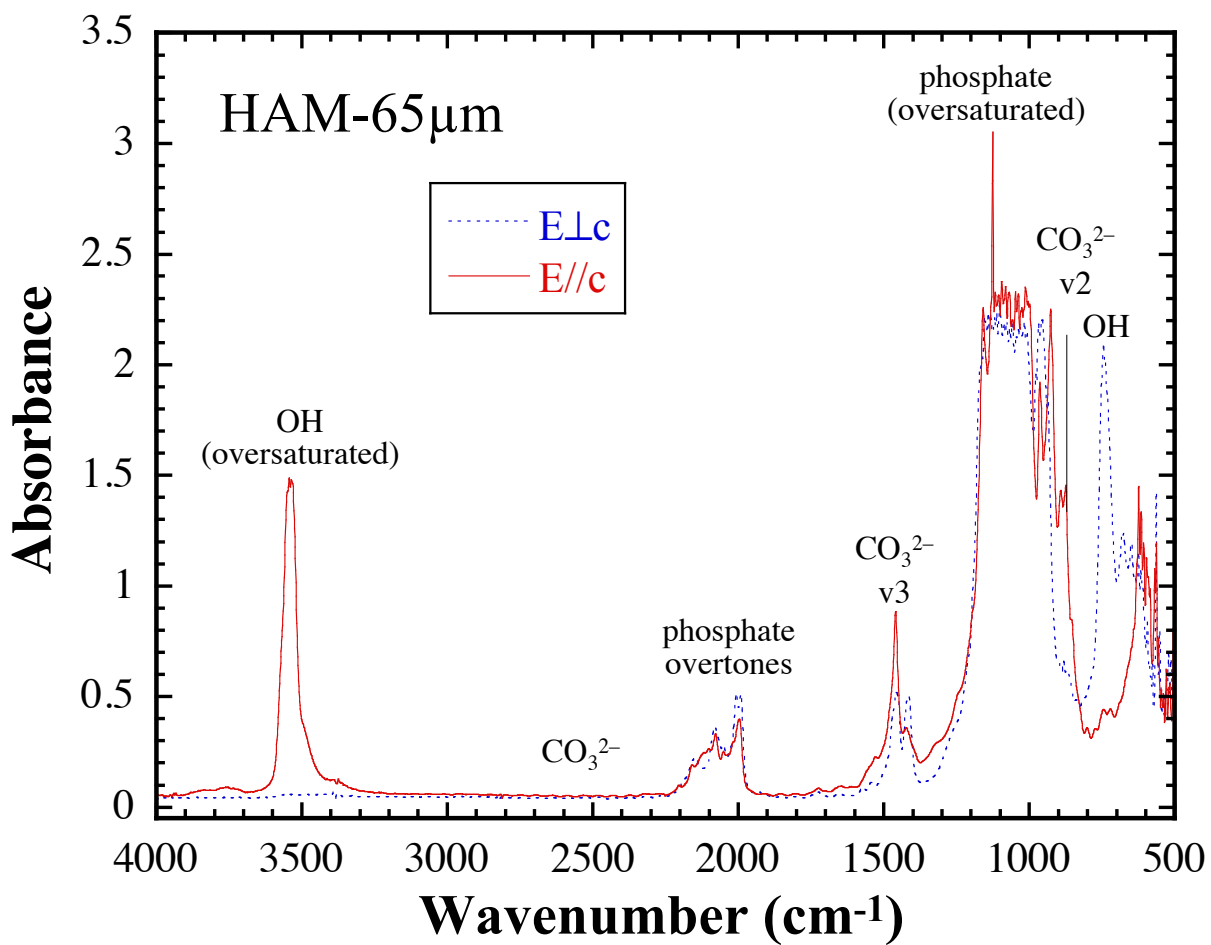
Fig. 2. Two polarized FTIR spectra for an apatite crystal from High Atlas Mountain (HAM), one for $\mathbf{E} \perp \mathbf{c}$ and one for $\mathbf{E} // \mathbf{c}$. The thickness of the crystal is 65 μm.
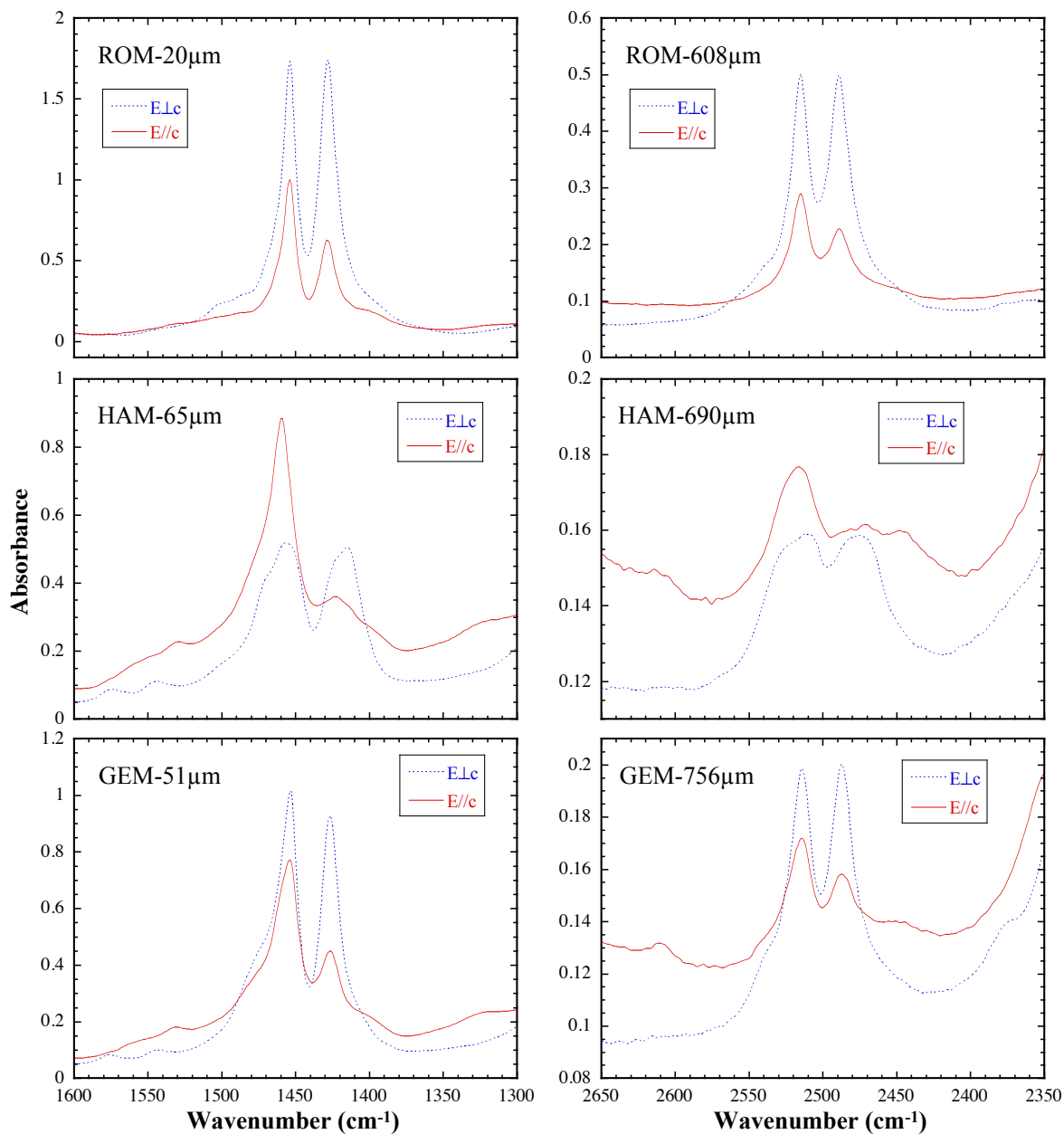
Figure 3. Polarized FTIR spectra at 1600-1300 cm^{-1} and 2650-2350 cm^{-1} collected from single apatite crystals. Note difference in this thickness of each sample, especially between wavenumber region of 1600-1300 cm^{-1} and of 2650-2350 cm^{-1}. To avoid oversaturation, the spectra at 1600-1300 cm^{-1} must be collected on very thin wafers. To get significant signal, the spectra at 2650-2350 cm^{-1} must be collected on thick wafers. The different shapes are due to different proportions of carbonate ions in A1, A2, B1 and B2 substitutions (see text).
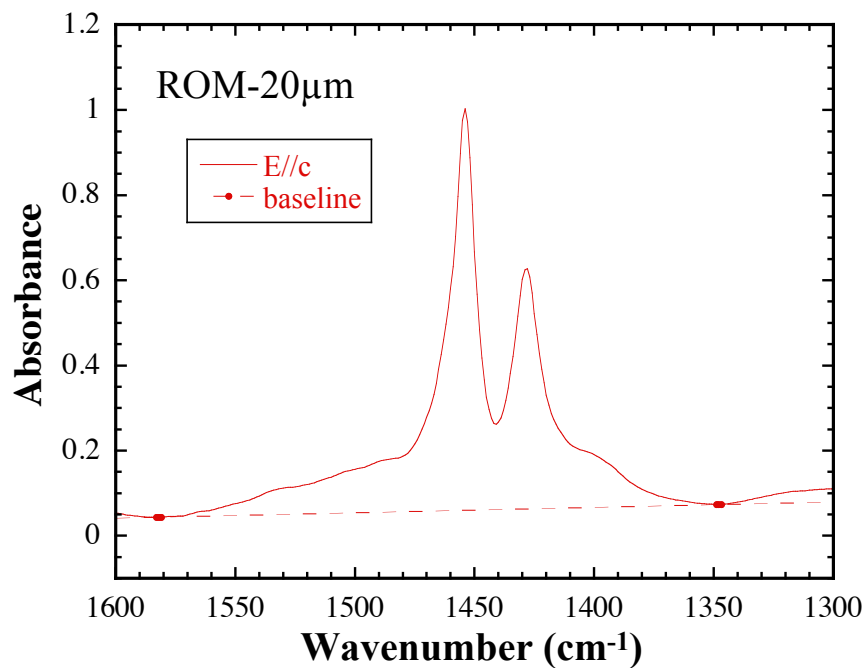
Figure 4. Illustration of baseline fitting for a polarized FTIR spectra
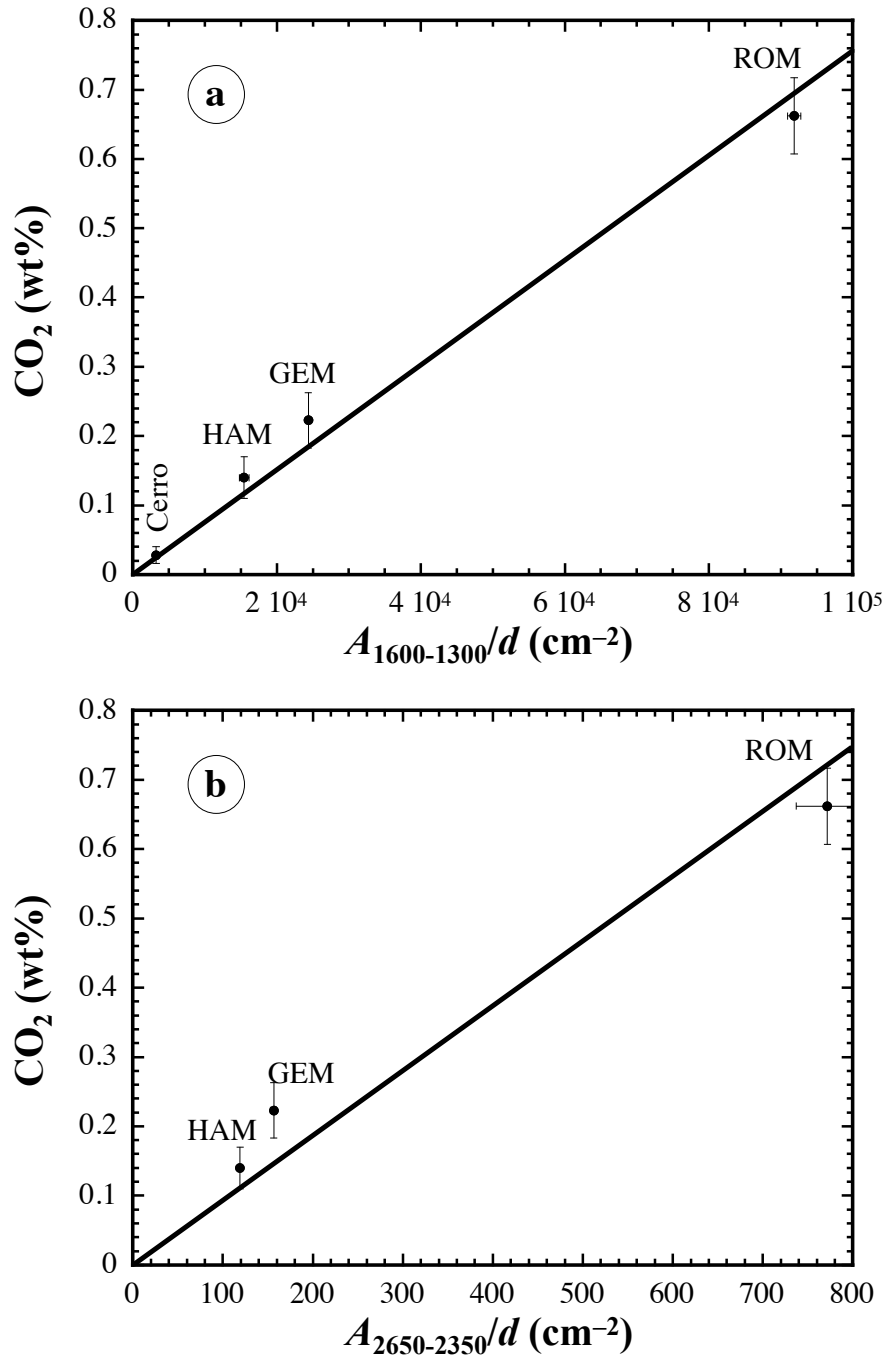at the v3 region (1600-1300 cm^{-1}) for **E⊥c** of a single apatite crystal ROM.

Figure 5. Calibration line for IR measurements of CO_2 in apatite. The integrated infrared absorbances are plotted on the horizontal axis. CO_2 concentrations determined by NRA are plotted on the vertical axis. The Cerro sample is plotted but not used in the fitting because it has already been used in estimating the background for NRA.
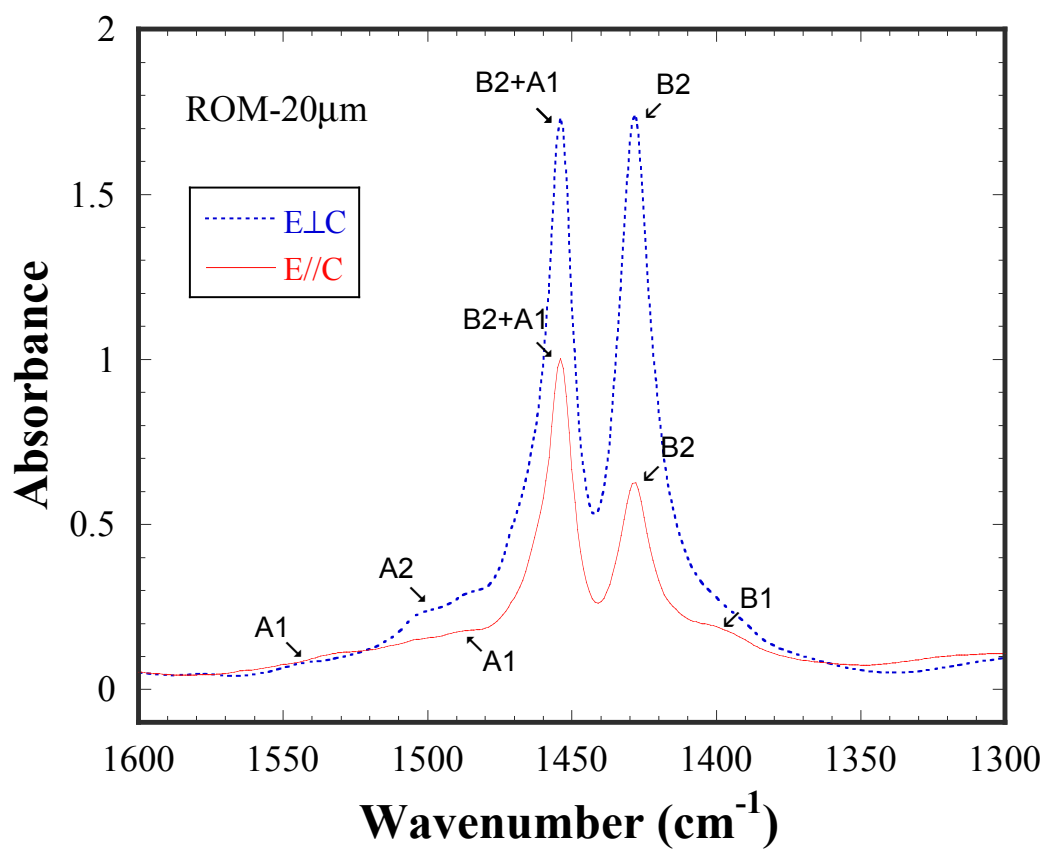
Figure 6. Polarized spectra illustrating the different peaks when **E^c** and when **E//c.**
A1 is the CO_2 substitution at the OH site and parallel to the c-axis of the crystal, A2 is perpendicular to the c-axis. B1 and B2 substitutions are on different faces of the PO_4 molecule (see text).